Revision 1

High temperature behavior of fluorcarletonite, $KNa_4Ca_4Si_8O_{18}(CO_3)_4(F,OH) \cdot H_2O$, from Murun Alkaline Complex (Russia) appraised by experimental and theoretical methods

Ernesto Mesto[1], Maria Lacalamita[1*], Ekaterina Kaneva[2,3], Roman Shendrik[2], Alexander Bogdanov[2], Marcello Merli[4], Emanuela Schingaro[1]

[1]Earth and Geoenvironmental Sciences Department, University of Bari Aldo Moro, via E. Orabona 4, I-70125 Bari, Italy; [2]Vinogradov Institute of Geochemistry, Siberian Branch of the Russian Academy of Sciences, 1a Favorsky Str., 664033 Irkutsk, Russia; [3]Sidorov Mineralogical Museum, Irkutsk National Research Technical University, 83 Lermontov Str., 664074 Irkutsk, Russia; [4]Earth and Sea Sciences Department, University of Palermo, via V. Archirafi 36, I-90123 Palermo, Italy

*corresponding author: maria lacalamita

e-mail: maria.lacalamita@uniba.it

Abstract

The thermal behavior of fluorcarletonite, $KNa_4Ca_4Si_8O_{18}(CO_3)_4(F,OH) \cdot H_2O$, from charoitites of the Severny district at the Malyy Murun massif (Murun complex, NW Aldan Shield, Siberia, Russia) has been investigated in order to understand the temperature-induced changes in the crystal structure of this rare silicate. The study has been carried out combining *in situ* high temperature single crystal X-ray diffraction (T range 25-550 °C), *ex situ* high temperature Fourier transform infrared spectroscopy (25-700 °C) and ab initio calculations. An increasing trend of lattice parameters and cell volume was observed in the 150-550 °C temperature range, when the mineral underwent a progressive dehydration process. At 550 °C about 40% water loss was detected. If compared with the fluorcarletonite structure at room temperature, the partially dehydrated fluorcarletonite shows: the same space group (*P*4/*mbm*); increased distances between the oxygens of the H_2O molecules (O11w and O12w) and their Na-centered octahedral cations (Na1 and Na2, respectively); distortion of the four- and six-member tetrahedral rings of the double silicate layer. The dehydration process mainly involves the oxygen at the O11w site which has a different local environment with respect to the oxygen at the O12w site. At $T > 600$ °C, the complete dehydration is accompanied by deprotonation of the OH groups substituting for the F atoms and by the collapse of the structure when the CO_2 is released. The adopted approach allowed to define the temperature thresholds at which modifications occur in the fluorcarletonite crystal structure subjected to controlled heating conditions. Our findings contribute to assess stability, reactivity and, more generally, the thermal behavior of sheet silicates with fluorcarletonite-like topology.

Keywords: fluorcarletonite, high temperature, single crystal X-ray diffraction, infrared spectroscopy, ab initio calculations.

Introduction

Fluorcarletonite, $KNa_4Ca_4Si_8O_{18}(CO_3)_4(F,OH) \cdot H_2O$, from Malyy Murun syenite massif (Aldan Shield, Siberia, Russia) was recently approved as a new mineral species as recognized by the official IMA-CNMNC List of Mineral Names (no. 2019-038). The first description of this mineral was provided by Kaneva *et al*. (2020a), who also explained the difference with respect to the structural analog carletonite, $KNa_4Ca_4Si_8O_{18}(CO_3)_4(OH,F) \cdot H_2O$ (Kaneva *et al*., 2023). The latter is a rare mineral named after Carleton University in Ottawa, found in the Poudrette quarry, Mont Saint-Hilaire, Canada (Chao 1971, 1972). Fluorcarletonite and carletonite undergo replacement of F ions with OH groups (or vice versa) which does not cause significant structural differences since the fluorine and OH radii are very close (1.30 and 1.36 Å, Shannon 1976) and the hydrogen does not significantly affect the local environment. The fluorine content in the crystal chemical formulas of fluorcarletonite varies in the range of 0.53-0.98 atoms per formula unit, apfu (Kaneva *et al*., 2020a, 2023) whereas for carletonite from Mont Saint-Hilaire massif F = 0.41 apfu (Chao 1971) or $0.36 \leq F \leq 0.41$ apfu (Kaneva *et al*., 2023) was reported.

In the peripheral regions of zoned grains of russian fluorcarletonite, carletonite composition has been detected (Kaneva *et al*., 2020a, 2022) so that, conversely fluorcarletonite might occur in the rocks of Mount Saint-Hilaire Massif (Canada). However, pure hydroxyl or fluorine end-members have not yet been found. The occurrence of carletonite in lateritic soils covering carbonatites, ijolites, nepheline syenites and fenites of the Bingo carbonate complex, Democratic Republic of Congo (Kasay 2018; Kasay *et al*., 2021) should also be confirmed by more accurate chemical and X-ray diffraction investigations.

Fluorcarletonite and carletonite are described as double-layer sheet silicates based on the $[4.8^2]_{16}$ net with an arrangement of upward-pointing tetrahedra (u) and downward-pointing tetrahedra (d) showing $(u^2d^2)_4(udududud)_4$ configuration and 1:2.25 T:O ratio (Hawthorne *et al*., 2019). In detail, $[Si_8O_{18}]^{4-}$ sheets, extending in the *a*-*b* plane, consist of four-member rings with two upward- and two downward-pointing tetrahedra, and eight-member rings with alternately

upward- and downward-pointing tetrahedra. Two adjacent single layers are interconnected by sharing a common oxygen of downward-pointing tetrahedra. The $[Si_8O_{18}]^{4-}$ sheets are connected with sheets consisting of $NaO_4^{2-}F^-(H_2O)$ and $NaO_5^{2-}(H_2O)$ octahedra, NaO_8^{2-}, $CaO_7^{2-}F^-$ or CaO_8^{2} and KO_{10}^{2-} polyhedra. The structural role of H_2O molecules is different, since one molecule is bonded to an interstitial cation and acts as a bond-valence transformer, the other one is non-transformer (Hawthorne 1992). Two independent CO_3-groups are linked to Na- and Ca-polyhedra.

The crystal structure of fluorcarletonite was determined experimentally at low temperature (100 K; Kaneva *et al*., 2020a) and room temperature, RT (Kaneva *et al*., 2023) but was also simulated in order to define the position of the hydrogens and the most energetically favorable orientations of the H_2O (Kaneva *et al*., 2023). The geometrical parameters of fluorcarletonite were found very similar to those of carletonite although they are distinct mineral species with individual peculiarities. In particular, the carletonite structure exhibits a splitting of the K atom over two sites, with 89% and 6% approximate occupancy, whereas the K position in fluorcarletonite is ordered (Kaneva *et al*., 2023).

In Kaneva *et al*. (2022, 2023) also the luminescence and the gemmological properties of fluorcarletonite were completely characterized. The multicolored appearance of the fluorcarletonite-containing rocks which is due to the association of various minerals, makes these samples very attractive gem materials for incorporation into jewelry and ornamental items (Kaneva *et al*., 2020a, 2022).

The thermal behavior of fuorcarletonite has not been thoroughly assessed. Chao (1971) studied the decomposition of carletonite by means of *ex situ* High Temperature X-ray Powder Diffraction (HT XRPD) analyses and Differential Thermal Analysis. The structure breakdown was associated to the release of CO_2 (but also of H_2O) evidenced by a strong endothermic peak in the DTA curve at 692 °C. Kaneva *et al*., (2020a) used thermogravimetric (TG) and differential scanning calorimetric (DSC) analyses on fluorcarletonite and found that the mineral underwent

dehydration from 45 to 315 °C, loss of CO_2 from 630 to 1134 °C and defluorination from 1136 to 1500 °C.

In the present study, the thermal behavior of fluorcarletonite was appraised via a combination of experimental (*in situ* High Temperature Single Crystal X-ray Diffraction, HT SCXRD; *ex situ* High Temperature Fourier Transform Infrared Spectroscopy, HT FTIR) and theoretical (ab initio simulations) methods, thus filling the gaps from previous studies and providing new insights into the structural variations of minerals with complex bond topology in relations to temperature changes.

Geological context and sample description

The studied fluorcarletonite occurs in charoitites of the Severny district at the Malyy Murun massif (Murun complex, NW Aldan Shield, Siberia, Russia). The ultra-agpaitic alkaline Murun complex was dated 137–128 Ma and had a complex geological history characterized by four igneous stages (early intrusive, main intrusive, volcanic, and late intrusive) and by hydrothermal activity represented by quartz veins with rutile–brookite–anatase mineralization (see more details in Vladykin 2009; Borovikov *et al*., 2018; Ivanov *et al*., 2018; Vladykin et al. 2018).

Kaneva et al. (2020a, 2022) carried out the mineralogical and petrographic examination of a polished slab of a fluorcarletonite-containing rock sample from the Malyy Murun massif and found that the mineral paragenesis is defined by the crystallization of alkali silicates (fluorcarletonite, charoite, apophyllite-(KF), aegirine, pectolite), quartz, apatite, and microcline, by the formation of copper and lead sulphides as well as native copper, and by the alteration of primary rock-forming minerals with formation of secondary apophyllite-(KF) and wollastonite caused by supergene conditions. Fluorcarletonite appears as allotriomorphic grains blue in color and forming close intergrowths with fluorapophyllite-(K) and pectolite.

In the present study, fluorcarletonite from the same rock sample as in Kaneva *et al*., (2020a, 2022, 2023) was considered. The authors reported for fluorcarletonite the following average crystal chemical formula $K_{0.99}Na_{3.86}Ca_{3.87}Sr_{0.02}Si_{7.99}Al_{0.01}O_{18}(CO_3)_{3.81}(F_{0.60}OH_{0.40})\cdot 1.42H_2O$.

Methods

In situ HT SCXRD

Single crystals of fluorcarletonite suitable for the X-ray diffraction investigation were selected under an optical microscope, glued on the tip of a glass fiber and mounted on a goniometer head. The *in situ* high temperature X-ray diffraction experiment was carried out with a Bruker AXS APEX II diffractometer equipped with MoKα radiation (λ = 0.71073 Å), a CCD area detector and a home-made heating device (Zema *et al*., 2022). A crystal (labelled Fcarl_1, 0.50 × 0.21 × 0.20 mm^3) with good diffraction behavior was heated in air from 25 to 450 °C in steps of 25 °C, with an heating rate of 1°C/min. After each heating step, the crystal was equilibrated for ca. 30 min before the acquisition of a new data collection. A total of eighteen data collections was acquired: those at 25 and in the T range 125-450 °C lasted ca. 6 hours ($2\theta_{max}$ = 66°, d_{hkl} = 0.65 Å) whereas those from 50 to 100 °C lasted 1 hour ($2\theta_{max}$ = 60°, d_{hkl} = 0.7 Å). The experiment was repeated by heating a second crystal (labelled Fcarl_2, 0.63 × 0.35 × 0.30 mm^3) from 25 to 550 °C with the same operating conditions. However, in this case all the data collections lasted ca. 1 hour ($2\theta_{max}$ = 72°, d_{hkl} = 0.60 Å). Attempts were also made to heat the Fcarl_2 crystal up to 625 °C but loss of crystallinity was observed.

The diffractometer operated at 50 kV and 30 mA. The collection strategies were optimized with the Apex program suite (Bruker 2010); data reductions were done using the software SAINT (Bruker 2007); empirical absorption corrections were applied using SADABS (Bruker 2009); structure refinements were performed with the program CRYSTALS (Betteridge *et al*., 2003) in the space group *P*4/*mbm* using reflections with $I > 3\sigma(I)$ and starting from the atomic coordinates of fluorcarletonite reported in Kaneva *et al*., (2023). The refined parameters were: scale factor,

atomic positions and anisotropic displacement parameters. The occupancies of the cation sites were constrained to 1 whereas the H_2O occupancies (O11w, O12w oxygen atoms) were refined for all the data collections. The analysis of the difference-Fourier maps evidenced the presence of residual electron density peaks less than 0.8 $e^-/Å^3$.

Details on data collections and structure refinements at 25, 100, 200, 300 and 450 °C for Fcarl_1 crystal, and at 25 and 550 °C for Fcarl_2 crystal are reported in Table 1. Selected bond distances at 25, 450 and 550 °C are provided in Table 2. Selected anion distances and angles are listed in Table 3. Crystallography Information Files of all the crystal structures refined for Fcarl_1 and those at 25 and 550 °C for Fcarl_2 are submitted as supplementary material together with atomic coordinates, site occupancy and displacement parameters at selected temperature (Table S1) and bond-valence data at 25 and 550 °C (Tables S2). Bond valence calculations were performed using the parameters from Brown and Altermatt (1985), and Breese and O'Keeffe (1991) for the cation–fluorine bonds.

Ex situ HT FTIR

Fourier transform infrared spectra were measured using an FT−801 spectrophotometer (Simex, Russia). Pelletized powdered samples were analyzed at a resolution of 2 cm^{-1} by collecting a total of 32 scans for each spectrum in the T range 25-700 °C. The *ex situ* experiment was performed by using the procedure described in previous publications (Kaneva *et al*., 2020b; Kaneva and Shendrik 2022) and briefly summarized as follows: (1) a mixture of fluorcarletonite and preliminarily dried pure KBr powder was pressed into a transparent tablet and heated to a target temperature for 5 minutes; (2) the same heating temperature and heating time were applied for pure dried KBr pellets, used as reference; (3) both the mixture and pure KBr pellets were cooled down to room temperature and the IR absorption spectra were measured again. These steps were repeated during the heating from 100 ºC up to 700 ºC.

Ab initio calculation

Ab initio modeling of IR spectra was carried out using the "VASP" ab initio code (Kresse and Hafner 1993), employing a pseudopotential method and plane wave basis sets. Exchange and correlation were expressed in terms of the PBEsol functional (Perdew *et al*., 2008), with an energy cutoff for plane wave basis sets of 400 eV. The Brillouin zone sampling was performed using gamma point only.

The geometry was relaxed until the maximal force acting on an atom was less than 0.001 eV/Å, followed by phonon calculation using the "Phonopy" code (harmonic approximation), Togo and Tanaka (2015). The infrared spectra were simulated with the "Phonopy−Spectroscopy" tool, with a single model containing fully populated O11w and O12w (six H_2O molecules) being calculated. The methodology of assigning the calculated modes has been described in detail in Bogdanov *et al*., (2021).

Because of the presence in the structure of hydrogens that can involve a significant anharmonicity, the above simulations have been coupled to ab initio molecular dynamics runs, carried out by means of the “Abinit” code (Gonze *et al*., 2016), with PBEsol for exchange and correlation functional, and energy cut off converged to 90 eV. NVT ensemble molecular dynamics calculations have been carried out at 27, 327 and 627 °C. For all the runs, the same (idealized) starting *P*1 geometry obtained from *ab-initio* modelling in Kaneva *et al.* (2023) has been adopted (with a = 13.2256 Å, c = 16.7329 Å, V = 2926.9 Å^3 and 226 atoms). Given the large unit cell and the consequent great number of atoms, no supercell has been adopted in the molecular dynamics simulations. The systems were equilibrated after 10^3 steps, with a time step of 2.5 fs.

Results

Crystal structure description at room and high temperature

Room temperature refinement in space group *P*4/*mbm* converged to R_1 = 3.34 % (for Fcarl_1) and 2.83 % (for Fcarl_2), wR_2 = 4.30 % (for Fcarl_1) and 3.14 % (for Fcarl_2), see Table 1. The values of the refined lattice parameters and cell volume were very close for the two studied crystals (*a* = 13.2077(4), *c* = 16.7234(5) Å, V = 2917.3(2) Å^3 for Fcarl_1 and *a* = 13.2082(3), *c* = 16.7219(4) Å, V = 2917.25(15) Å^3 for Fcarl_2, Table 1) and similar to those in Kaneva *et al*. (2023).

A representation of the complete crystal structure of fluorcarletonite, plotted down the *b* axis, is given in Fig 1. It consists of two tetrahedral sites (*Si*1 and *Si*2), two octahedral independent sites (*Na*1 and *Na*2), two 8-coordinated sites (*Na*3 and *Ca*1), one 10-coordinated site (*K*1), two 3-coordinated sites (*C*1 and *C*2), ten oxygen sites, one F site and two sites occupied by oxygens of H_2O (O11w and O12w sites), Fig. 1 and Table S1. Figure 2, instead, displays a fragment of the fluorcarletonite crystal structure with details on the local environment of the oxygen at the O11w and O12w sites.

The refined occupancies for the oxygens at the O11w and O12w sites at RT were, respectively, 0.93(2) and 0.62(3) for the Fcarl_1, and 1.016(17) and 0.650(19) for Fcarl_2 (Table S1). Similar values were found in previous investigations for fluorcarletonite (O11w = 0.833(9) and O12w = 0.535(9) in Kaneva *et al*., 2020; O11w = 0.87(1) and O12w = 0.55(2) in Kaneva *et al*., 2023) as well as for carletonite (Chao 1972; Kaneva *et al*., 2023). The $U_{iso/equivalent}$ values of oxygens at the O11w and O12w sites are larger than those of all other atoms (Table S1), consistently with their low BVS (Table S2). The thermal motion for these oxygens is particularly pronounced already at room temperature. A similar behavior was also observed in the case of other hydrated sheet silicates with complex bond topology (Lacalamita *et al.* 2023).

In addition, short O12w-O12w distance (1.95(4) Å, Table 3) confirms the occurrence of mutually exclusive positions of nearest oxygens at the O12w site (Kaneva *et al*., 2023). The values of individual and average bond length distances for tetrahedra, Na- and Ca-polyhedra of the studied crystals (Table 2) were also very similar to those reported in the literature.

229 Given the close similarities in the geometrical features of the two studied crystals, in the text
230 below and in the figures, we will consider the data collected at 550 °C for Fcarl_2 in addition to
231 those from 25 to 450 °C for Fcarl_1.
232 With increasing temperature, fluorcarletonite does not show change in symmetry (Table 1).
233 However, the evolution of the normalized unit cell parameters and volume as a function of the
234 temperature (Fig.s 3 and S1) evidences that the unit cell dimensions remain almost constant until
235 ~ 150-200 °C when they start to increase.
236 Figure 4 shows that the mean atomic number of the oxygen at O12w and especially at the O11w
237 site progressively decrease as the temperature increases. Considering that correlation coefficient
238 between occupancies and Uij's of O11w and O12w are < 0.6 both for RT and 550°C
239 measurements, these results point to an overall dehydration of fluorcarletonite at 550 °C of ~
240 40%.
241 The oxygen at the O11w site coordinates the Na1 octahedron together with four O3 atoms of the
242 silicate layer and one F. It points towards an equivalent O11w oxygen, both lying on the *c* axis
243 (Fig. 2). During heating, the *Na*1-O11w bond weakens (0.229 vu and 0.119 vu at 25 and 550 °C,
244 respectively, Table S2). In detail, the oxygen moves away from the *Na*1 neighboring cation (as
245 indicated by the lengthening of the *Na*1-O11w distance from 2.349(7) to 2.59(3) Å, Table 2) and
246 approaches the equivalent O11w oxygen (as testified by the shortening of the O11w-O11w'
247 distance from 2.822(13) to 2.26(6) Å, Table 3).
248 The O12w is shared by two *Na*2 octahedra which are also bonded to one O4 atom of the silicate
249 layer, two O7 and two O10 atoms (Fig. 2). The oxygen at O12w receives 0.054 vu at RT and
250 0.026 vu at 550 °C (Table S2). The water content at the O12w site slightly decreases (from 4.96
251 to 3.84 m.a.n.'s, e^- at RT and 550 °C, respectively, Fig. 4) while the distance of the oxygen at
252 O12w site from the *Na*2 neighboring cation strongly increases (from 2.886(3) Å at RT to 3.16(2)
253 at 550 °C, respectively, Table 2). At the same time, the O12w-O12w' distance decreases (from
254 1.95(4) at RT to 1.28(7) at 550 °C, respectively, Table 3, Fig. 2).

No significant modifications of the geometrical parameters of the *Na*3-, *Ca*1-, and *K*1-polyhedra as well as of the CO_3 groups at 550 °C with respect to RT are observed (Table 2).

As concern the tetrahedral framework, Fig. 2 shows that the linkage between two single tetrahedral layers via the oxygen at the O6 site defines, in the *a*-*c* plane, four- and six-membered tetrahedral rings alternated along *a* and with a mean area 4.0047(37) x 3.2213(38) $Å^2$ and 5.1720(28) x 4.4858(37) Å, respectively, at RT (Fig. 2a). As the temperature increases, a distortion of these rings is observed. In particular, the stretching of the *Si*1 tetrahedra along the *c* direction causes an increment of the O5-Ô6-O5 angle (from 75.188(63) to 81.029(86)° at RT and 550 °C, respectively, Table 3) and, consequently, an elongation of the four-membered tetrahedral rings along the *c* direction together with its compression along the *a* direction. On the contrary, the adjacent six-membered tetrahedral ring expands in the *a* direction (compare Figs. 2a and 2b). A tilting of the *Si*2 tetrahedra has also been observed as revealed by the O2-Ô1-O3 angle increment from 100.429(87) at 25 °C to 102.028(116) at 550 °C (Table 3).

High temperature infrared data

The infrared spectra of fluorcarletonite heated from RT to 700 °C are presented in Figs. 5 and 6 for the Si–O framework and the O-H stretching vibration regions, respectively.

At low frequencies, weak bands between 500 and 900 cm^{-1} are observed in the spectrum collected at RT (Fig. 5). By increasing the temperature, the bands at 526, 591 and 661 cm^{-1} shift and at T = 700 °C are found centered at 519, 586 and 655 cm^{-1}, respectively (Fig. S2). The intensity of the bands at 591 and 693 cm^{-1} decreases; the latter trend is also observed for the absorption band in the 802-815 cm^{-1} range which at $T > 400$ °C shows a maximum at 808 cm^{-1}. No changes affect the bands at 701, 729, 785 and 875 cm^{-1}.

At higher frequencies, a strong band occurs at 1050 cm^{-1} as also reported elsewhere (Kaneva et al. 2020a) but it is not shown in Fig. 5. The band at 1196 cm^{-1} splits into two bands at 1170 and 1220 cm^{-1} starting from T = 500 °C. Bands peaked at 1397, 1418, 1451, 1480 and 1525 cm^{-1}

281 with shoulders at 1371 and 1550 cm^{-1} change their shape during heating (Fig. 5). In particular,
282 the bands at 1418 and 1480 cm^{-1} become less resolved at T = 600 °C, and the intensities of the
283 1397 and 1451 cm^{-1} bands slightly decrease.
284 In the O-H stretching region three main peaks at 3557, 3582 and 3645 cm^{-1} (with a shoulder at
285 3595 cm^{-1}) are observed at RT (Fig. 6). In the spectra of the annealed fluorcarletonite, the
286 intensity of the peaks at 3557 and 3645 cm^{-1} progressively decreases until they vanish at $T > 200$
287 and 500 °C, respectively. This evolution makes more evident a peak centered at 3690 cm^{-1}
288 starting from T = 200 °C. At the same temperature a band centered at 3595 cm^{-1} appears. This
289 band together with that at 3582 cm^{-1} shows only minimal changes during heating. Overall, the
290 OH stretching bands may be hardly detected at T = 600 °C. The temperature dependences of
291 these band intensities are given in Fig. S3.
292 In Fig. 6 very low intensity bands at 2950, 3015 and 3420 cm^{-1} are also shown. The wide
293 absorption at 3420 cm^{-1} disappears after T = 100 °C while intensity and position of the bands at
294 2950 and 3015 cm^{-1} remains unchanged in the whole explored temperature range.
295
296 **Discussion**
297 *Structural evolution under high temperature*
298 The *in situ* high temperature X-ray diffraction experiment from 25 to 550 °C on fluorcarletonite
299 (Murun massif, Russia) evidenced that the mineral undergoes a thermal expansion of the unit cell
300 volume accompanied by a progressive dehydration. In layered minerals the removal of interlayer
301 H_2O molecules and the reorganization of the interlayer space usually results in a decrease in the
302 *d*-spacing and, as a consequence, in the shrinking of the unit cell parameters and volume
303 contraction (Bray *et al*., 1998; Zema *et al*., 2009; Post *et al*., 2015). However, in some hydrated
304 sheet silicates with complex bond topology, the tetrahedral framework defines interlayer cavities
305 hosting zeolitic H_2O molecules and/or alkaline cations (e.g. McDonald and Chao 2009;
306 Lacalamita *et al*., 2023). In particular, in fedorite, $(K,Na)_{2.5}(Ca,Na)_7Si_{16}O_{38}(OH,F)_2 \cdot 3.5H_2O$, the

307 tetrahedral rings of the $[Si_{16}O_{38}]^{12-}$ unit intrude the interlayer space thus hampering, during
308 heating, the release of H_2O molecules (Lacalamita *et al*., 2023). As a consequence, the partial
309 dehydration of the mineral involves only a slight cell volume contraction (Lacalamita *et al*.,
310 2023). The crystal structure of fluorcarletonite may be related to that of fedorite since in both
311 silicates two tetrahedral single layers are linked by an apical oxygen atom (see Fig. 2 in
312 Lacalamita *et al*., 2023 and Fig. 1, this study). However, fluorcarletonite does not contain
313 zeolitic water. The mineral has two independent crystallographic sites occupied by the oxygens
314 of H_2O molecules coordinating Na-centered octahedra and showing very different local
315 environments (Fig. S4). In detail, the oxygen at the O11w site is located in a cavity defined by
316 two overlapped eight-member rings while the oxygen at the O12w site is shared by two
317 octahedra and statistically distributed on two symmetrically equivalent sites (O12w and O12w'),
318 as stated above. The oxygen at the O11w site points toward the double tetrahedral layers and is
319 bonded only to cation at *Na*1 (Table S2). This explains its capability to shift along the *c* axis by
320 moving away from the Na atom and leave the crystal structure under heating conditions. Almost
321 one half of the water content at the O11w site was, indeed, observed at 550 °C with respect to
322 that found at RT (Fig. 4; Table S1).
323 The oxygen at the O12w site moves toward the equivalent position at O12w' (Table 3) and, as a
324 consequence, it approaches the two symmetrically equivalent *Na*2'-octahedra (Fig. 2). The
325 bonding of the oxygen at the O12w site may be also affected by the cations at the *Na*2' sites.
326 Despite a reduction of the bond valence sum at the O12w site was observed from 25 to 550 °C
327 (Table S2), negligible changes in BVS actually affect the O12w site if the contribution of the
328 *Na*2' ion bond strengths is considered. This hypothesis also is in keeping with the slight decrease
329 of the occupancy observed at the O12w site (Fig. 4; Table S1).
330 Therefore, fluorcarletonite upon heating to 550 °C undergoes dehydration which is accompanied
331 by a substantially isotropic enlargement of the unit cell parameters (Δa = 0.53 %; Δc = 0.55 %)
332 and expansion of the unit-cell volume (ΔV = 1.6 %). Its behavior resembles that of framework

silicates, specifically, of zeolites where the dehydration is not accompanied by significant changes in the framework structure and unit cell volume (Arletti *et al.*, 2018).

Vibrational features upon heating

The assignment of the infrared bands in Figs. 5 and 6 was performed using *ab initio* calculations (Table 4).

Focusing on the tetrahedral framework, the prominent band at 1050 cm^{-1} (not shown in Fig. 5) and the less intense one at 1196 cm^{-1} are associated with Si−O stretching vibrations. The splitting of the latter band is ascribed to the thermal expansion of the tetrahedral framework during annealing. The SiO_4 bending vibrations are affected by H_2O libration modes. In detail, the shifts detected for the 526, 591 and 661 cm^{-1} bands correlates well with temperature changes and are due to the dehydration (Fig. S2). The same reason explains the variation in shape of the band in the 802-815 cm^{-1} range, likely due to the change in the position of the O11w and O12w atoms during heating.

Regarding the $(CO_3)^{2-}$ anions, the less intense band at 875 cm^{-1} may be associated to the out-of-plane bending of $(CO_3)^{2-}$. The two non-equivalent groups of $(CO_3)^{2-}$ anions have a distorted D3h point group. Therefore, at least five bands (1371-1527 cm^{-1}, Fig. 5) correspond to asymmetric stretching modes of the $(CO_3)^{2-}$ anions. In detail, ab initio calculations indicate that the bands at 1397 and 1480 cm^{-1} are attributed to asymmetric stretching modes of $(C2O_3)^{2-}$, while the bands at 1418 and 1451 cm^{-1} are related to $(C1O_3)^{2-}$. At 1525 cm^{-1} the separate closed asymmetric vibrational modes of $(C1O_3)^{2-}$ and $(C2O_3)^{2-}$ anions are not well resolved. However, the change in the angle between $(C1O_3)^{2-}$ and the *b*-*c* plane leads to a decrease in the oscillator strength of this band. This rotation and subsequent disorder of $(C1O_3)^{2-}$ anions could also explain the widening of $(C1O_3)^{2-}$ related bands. Also the $(C2O_3)^{2-}$ disorder associated with the shoulder at 1371 cm^{-1} result from the dehydration process. On the other hand, the *C* atoms trajectories (Figs.

S5 and S6) obtained from the molecular dynamic simulation suggest the usual direction of vibration of C atoms, typically perpendicular to the CO_3 plane, for both *C*1 and *C*2 atoms. Finally, the stretching vibration of the OH groups replacing fluorine provide the band at 3690 cm^{-1} that become detectable at T = 200 °C and disappears at $T > 500$ °C (Fig. 6; Fig. S3, curve 4) whereas the Si−O−H silanol groups give rise to the bands at 2950 and 3015 cm^{-1} that are unaffected by heating.

The adsorbed surface H_2O molecules are lost at low annealing temperature (see the evolution of the band at 3420 cm^{-1}, in Fig. 6) whereas the structural H_2O molecules (associated to O11w and O12w) are responsible for the band at 591 cm^{-1} (libration mode) and for the shoulder at 1550 cm^{-1} (bending mode), see Fig. 5. The trajectories of the H atoms during annealing (see the deposited netCDF files) corroborate the occurrence of strong libration of the O11w and O12w. The O11w−H groups (stretching vibration at 3557 cm^{-1}, Fig. 5) undergoes deprotonation at $T >$ 200 °C (Fig. S3, curve 1). The released protons interact with other oxygen atoms, mainly the O6 forming new O-H bonds whose vibrations entail the appearance of the band at 3595 cm^{-1} at $T =$ 200°C that remains stable up to 500 °C (Fig. S3, curve 3). The temperature behavior of the 3595 cm^{-1} band (Fig. S3, curve 3) is similar to that of the band at 3690 cm^{-1} (Fig. S3, curve 4). The O12w−H (stretching vibration at 3645 cm^{-1}) deprotonate at $T > 600$ °C (Fig. S3, curve 2). The molecular dynamics results confirm the partial dehydration of the structure as indicated by the H atoms trajectories (Fig. S7), as well as by the Pair Distribution Function g(*r*) of the H atoms (Fig. S8). Indeed, the g(*r*) pattern at 27 °C actually differs from that at 327 or 627 °C when the dehydration is taking place. The first peak for the T = 27 °C case, centered around ≈1.2 Å, corresponds to the nearest neighbor shell for the O-H pair. This isolated peak (the probability g(*r*) drop to zero in the *r* range of ≈1.3-1.6 Å) for the T = 27 °C simulation is centered around the preferential distance between O and H atoms, that actually bind covalently, with small-amplitude vibrations around the equilibrium positions and with diffusive movements confined over small local regions, as suggested by the small spread of the peak. At higher temperatures this PDF

feature fails, and g(r) in the 1.3<r<1.6 Å range is significantly different from zero, suggesting that random collisions between particles and great positional disorder take place. This fact is also compatible with the trends shown by the values of the mean squared displacement (msd) of the H atoms vs. time at 27, 327 and 627 °C as depicted in Fig. S7: here, the high temperature patterns are those typically determined by significant self-diffusivity, while the T = 27 °C case clearly shows no diffusion at all for the H atoms.

The molecular dynamics also suggest that at 327 °C some of the released H atoms (coming from the O11w-H couples) form new bonds with oxygens, mainly the O6 atoms, thus producing a kind of "isomerism", i.e., rapidly interconverting isomers. The dehydrated O11w can re-interact with an H to form a new temporary OH bond. Two snapshots of the structures at 27 and 327 °C during the molecular dynamics runs after 1.8 ps and 1 ps respectively have been shown in Fig.s S9 and S10, respectively, while Table S3 can be used for better understanding of the bond setup evolution increasing temperature from 27 to 327 °C.

Conclusions

At elevated temperatures the crystal structure of fluorcarletonite undergoes dehydration and structural modifications whose knowledge may contribute to comprehend the stability of the mineral.

Under the adopted experimental conditions, the crystal structure of fluorcarletonite is stable from RT up to ~ 150-200 °C when the mineral starts to progressively dehydrate until about 550 °C. The present study allows to elucidate the mechanism of dehydration, that takes place in two stages since it firstly involves the oxygen at the O11w site (at ~ 150 ≤ T ≤ 550 °C) and, successively, interests the oxygen at the O12w site (mainly at T > 500 °C). In addition, ab initio calculations highlight a surprising behavior of the protons which may depart from the O11w-H groups linking with nearest oxygens thus leading to perturbations of the Si-O bonds in the double tetrahedral layer.

410 At a temperature above 500 °C also the OH groups substituting the F atoms leave the crystal
411 structure. Release of CO_2 at $T > 630$ °C and defluorination at $T > 1136$ °C (TG-DSC data by
412 *Kaneva et al*., 2020a) lead to the structure breakdown of fluorcarletonite as testified by the
413 amorphization of the single crystal during the *in situ* HTXRD experiment. Chao (1972) also
414 observed amorphization of carletonite quenched from 708 °C by associating the collapse of the
415 crystal structure to the loss of H_2O and CO_2. Defluorination of carletonite was reported to occur
416 at much lower temperature (300 °C, see Chao 1972) with respect to that found for
417 fluorcarletonite (Kaneva *et al*., 2020a).
418 The diffraction pattern of carletonite quenched from 775 °C revealed the characteristic peaks of
419 wollastonite ($CaSiO_3$), albite ($NaAlSi_3O_8$), $Na_2Ca_2Si_3O_9$ and $Na_2CaSi_3O_8$ (Chao 1972).
420 Wollastonite was also recognized as alteration product of primary minerals in the
421 fluorcarletonite-hosted rock under supergene conditions (Kaneva *et al*., 2022).
422 The data of the present study can be integrated into a more general framework of investigations
423 of the response to heating of a set of silicates with complex bond topology. The latter
424 annoverate, for instance, double-layer sheet silicates, i.e. the one based on 6^3 and 4.8^2 net,
425 according to the silicate minerals hierarchy of Hawthorne *et al*. (2019). Indeed, fedorite (6^3 net,
426 Hawthorne *et al*., 2019) was recently examined (Lacalamita *et al*., 2023) and was found to
427 exhibit a thermal behavior very similar to that of fluorcarletonite (4.8^2 net, Hawthorne *et al*.,
428 2019). Therefore, it is reasonable to expect that the tetrahedral framework topology prevents the
429 total H_2O migration also in other hydrated phases e.g. lalondeite
430 $(Na,Ca)_6(Ca,Na)_3[Si_{16}O_{38}]F_2(H_2O)$, macdonaldite $BaCa_4[Si_{16}O_{36}(OH)_2](H_2O)_{10}$, monteregianite-
431 Y $KNa_2Y[Si_8O_{19}](H_2O)_5$, seidite-Ce $Na_4Ce_2Ti[Si_8O_{22}](OH)(H_2O)_5$ of the group.
432 Further implications of our study concern technological applications. Indeed, changes in the
433 crystal structure of fluorcarletonite under high-temperature can lead to alterations in the
434 absorption spectra, as well as other optical characteristics. These modifications are of utmost

importance for the development of advanced optical materials, including light-emitting diodes, lasers, and optical sensors, with tailored properties.

Acknowledgments. This work was supported by a M. Lacalamita grant (SIMP 2020 Research Grant in Crystal-chemistry, in memory of Prof. Fiorenzo Mazzi). The Structures Editor Peter Leverett and two anonymous referees are gratefully acknowledged for their insightful suggestions.

Supplemental material

Figures S1-S10, Tables S1-S3 and Crystallography Information Files have been deposited with the Principal Editors of *Mineralogical Magazine* and are available as Supplementary material.

Competing interests. The authors declare none.

References

Arletti R., Fantini R., Giacobbe C., Gieré R., Vezzalini G., Vigliaturo R. and Quartieri S. (2018) High-temperature behavior of natural ferrierite: In-situ synchrotron X-ray powder diffraction study. *American Mineralogist*, **103**, 1741-1748.

Betteridge P.W., Carruthers J.R., Cooper R.I., Prout K. and Watkin D.J. (2003) Crystals version 12: software for guided crystal structure analysis. *Journal of Applied Crystallography*, **36**, 1487.

Bogdanov A., Kaneva E. and Shendrik R. (2021) New insights into the crystal chemistry of elpidite, $Na_2Zr[Si_6O_{15}]\cdot 3H_2O$ and $(Na_{1+y}Ca_x\square_{1-x-y})_{\Sigma=2}Zr[Si_6O_{15}]\cdot(3\text{-}x)H_2O$, and ab initio modeling of IR spectra. *Materials*, **14** (9), 2160.

Borovikov A.A., Vladykin N.V., Tretiakova I.G. and Dokuchits E.Yu (2018) Physicochemical conditions of formation of hydrothermal titanium mineralization on the Murunskiy alkaline massif, western Aldan (Russia). *Ore Geology Reviews*, **95**, 1066-1075.

461 Bray H.J., Redfern S.A.T. and Clark S.M. (1998) The kinetics of dehydration in Ca-
462 montmorillonite: an in situ X-ray diffraction study. *Mineralogical Magazine*, **62** (5), 647-656.
463 Brese N.E. and O'Keeffe M. (1991) Bond-valence parameters for solids. *Acta*
464 *Crystallographica,* **B47**, 192-197.
465 Brown I.D. and Altermatt D. (1985) Bond-valence parameters obtained from a systematic
466 analysis of the Inorganic Crystal Structure Database. *Acta Crystallographica*, **B41**, 244-247.
467 Bruker (2007) SAINT, Bruker AXS Inc., Madison, Wisconsin, USA.
468 Bruker (2009) SADABS, Bruker AXS Inc., Madison, Wisconsin, USA.
469 Bruker (2010) APEX2 v.2010.7-0, Bruker AXS Inc., Madison, Wisconsin, U.S.A.
470 Chao G. Y. (1971). Carletonite, $KNa_4Ca_4Si_8O_{18}(CO_3)_4(F,OH) \cdot H_2O$, a new mineral from Mount
471 St. Hilaire, Quebec. *American Mineralogist*, **56**, 1855-1866.
472 Chao G. Y. (1972). The crystal structure of carletonite, $KNa_4Ca_4Si_8O_8(CO_3)_4(F,OH) \cdot H_2O$, a
473 double-sheet silicate. *American Mineralogist*, **57**, 765-778.
474 Gonze X., Jollet F., Abreu Araujo F., Adams D., Amadon B., Applencourt T., Audouze C.,
475 Beuken J.-M., Bieder J., Bokhanchuk A., Bousquet E., Bruneval F., Caliste D., Côté M., Dahm
476 F., Da Pieve F., Delaveau M., Di Gennaro M., Dorado B., Espejo C., Geneste G., Genovese L.,
477 Gerossier A., Giantomassi M., Gillet Y., Hamann D.R., He L., Jomard G., Laflamme Janssen J.,
478 Le Roux S., Levitt A., Lherbier A., Liu F., Lukačević I., Martin A., Martins C., Oliveira M.J.T.,
479 Poncé S., Pouillon Y., Rangel T., Rignanese G.-M., Romero A.H., Rousseau B., Rubel O.,
480 Shukri A.A., Stankovski M., Torrent M., Van Setten M.J., Van Troeye B., Verstraete M.J.,
481 Waroquiers D., Wiktor J., Xu B., Zhou A. and Zwanziger J.W. (2016) Recent developments in
482 the ABINIT software package. *Computer Physics Communications*, **205**, 106-131.
483 Hawthorne F.C. (1992) The role of OH and H_2O in oxide and oxysalt minerals. *Zeitschrift für*
484 *Kristallographie*, **201**, 183–206.
485 Hawthorne F.C., Uvarova Y.A. and Sokolova E. (2019) A structure hierarchy for silicate
486 minerals: sheet silicates. *Mineralogical Magazine*, **83**, 3-55.

Ivanov A.V., Vladykin N.V., Demonterova E.I., Gorovoy V.A. and Dokuchits E.Y. (2018) $^{40}Ar/^{39}Ar$ geochronology of the Malyy (Little) Murun massif, Aldan shield of the Siberian craton: A simple story for an intricate igneous complex. *Minerals*, **8**, 602.

Kaneva E. and Shendrik R. (2022) Thermal behavior of natural stellerite: high-temperature X-ray powder diffraction and IR spectroscopy study. *Analytical Sciences*, **38**, 1523-1532.

Kaneva E., Radomskaya T., Suvorova L., Sterkhova I. and Mitichkin, M. (2020a) Crystal chemistry of fluorcarletonite, a new mineral from the Murun alkaline complex (Russia). *European Journal of Mineralogy*, **32**, 137-146.

Kaneva E., Bogdanov A. and Shendrik R. (2020b) Structural and vibrational properties of agrellite. *Scientific Reports*, **10** (1), 15569.

Kaneva E., Radomskaya T. and Shendrik R. (2022) Fluorcarletonite – a new blue gem material. *Journal of Gemmology*, **38** (4), 342-351.

Kaneva E., Bogdanov A., Radomskaya T., Belozerova O. and Shendrik R. (2023) Crystal-chemical characterisation and spectroscopy of fluorcarletonite and carletonite. *Mineralogical Magazine*, **87**, 356-368.

Kasay GM. (2018) *Geology, geochemistry and economic potential of the Bingo carbonatite and its associated laterites in Beni, North Kivu, Democratic Republic of Congo (DRC)*. PhD dissertation, University of Nairobi, Kenya.

Kasay G.M., Bolarinwa A.T., Aromolaran O.K., Nzolang C. and Mambo V.S. (2021) A review of the geological settings, ages and economic potentials of carbonatites in the Democratic Republic of Congo. *Applied Earth Science*, **130**, 143-160.

Kresse G. and Hafner J. (1993) Ab initio molecular dynamics for liquid metals. *Physical review B*, **47** (1), 558-561.

Lacalamita M., Mesto E., Kaneva E., Shendrik R., Radomskaya T. and Schingaro E. (2023) High temperature behavior of fedorite, $Na_{2.5}(Ca_{4.5}Na_{2.5})[Si_{16}O_{38}]F_2 \cdot 2.8H_2O$, from the Murun Alkaline Complex, Russia. *Mineralogical Magazine*, **87** (4), 542-553.

McDonald A. and Chao G.Y. (2009) Lalondeite, a new hydrated Na–ca fluorosilicate species from Mont Saint-Hilaire, Quebec: description and crystal structure. *The Canadian Mineralogist*, **47**, 181-191.

Perdew J.P., Ruzsinszky A., Csonka G.I., Vydrov O.A., Scuseria G.E., Constantin L.A., Zhou X. and Burke K. (2008). Restoring the density-gradient expansion for exchange in solids and surfaces. *Physical Review Letters*, **100** (13), 136406.

Post J.E., Bish D.L. and Heaney P.J. (2015) Synchrotron powder X-ray diffraction study of the structure and dehydration behavior of sepiolite. *American Mineralogist*, **92**, 91-97.

Shannon R.D. (1976) Revised effective ionic radii and systematic studies of interatomic distances in halides and chalcogenides. *Acta Crystallographica*, **A32**, 751-767.

Togo A. and Tanaka I. (2015). First principles phonon calculations in materials science. *Scripta Materialia*, **108**, 1-5.

Vladykin N.V. (2009) Potassium alkaline lamproite-carbonatite complexes: Petrology, genesis, and ore reserves. *Russian Geology Geophysics*, **50**, 1119-1128.

Vladykin N.V., Borokovikov A.A., Dokuchits E.Yu. and Thomas V.G. (2018) Genesis of charoite rocks in the Murun massif, Aldan Shield, Russia. *Geochemistry International*, **56**, 1135-1147.

Zema M., Ventruti G., Lacalamita M. and Scordari F. (2010) Kinetics of Fe-oxidation/deprotonation process in Fe-rich phlogopite under isothermal conditions. *American Mineralogist*, **95**, 1458-1466.

Zema M., Ventruti G., Tarantino S. and Micelli C. (2022) A new thermal and atmospheric conditioning device for in situ single-crystal diffraction is up and running. S18-21 in: *Book of abstract of the congress on Geosciences for a sustainable future*. Società Geologica Italiana e Società Italiana di Mineralogia e Petrologia, Torino, Italy.

FIGURE CAPTIONS

539 **Fig. 1.** Crystal **s**tructure of fluorcarletonite from Murun Massif as seen along *b*. Si-tetrahedra
540 (orange), Na-polyhedra (blue), Ca-polyhedron (pink), K^+ (brown) and C (grey) atoms are
541 represented. Oxygen and fluorine atoms are illustrated in red and green, respectively.
542 **Fig. 2.** Detail of the crystal **s**tructure of fluorcarletonite showing the dimensions of the tetrahedral
543 rings in the *a*-*c* plane at (a) T = 25 °C (b) T = 550 °C. Colors as in Fig. 1.
544 **Fig. 3.** Normalized unit cell parameters and volume of Fcarl_1 crystal *versus* temperature.
545 Symbols: a/a_0 and b/b_0 (light grey); c/c_0 (dark grey); V/V_0 (black). a_0, b_0, c_0, and V_0 are lattice
546 parameters and unit cell volume at RT, respectively. The size of the symbols is larger than the
547 associated esd's.
548 **Fig. 4.** Mean atomic numbers (m.a.n.'s, e^-) at the oxygens at O11w (dark gray line and symbol)
549 and O12w sites (light gray line and symbol) in fluorcarletonite *versus* temperature.
550 **Fig. 5.** IR absorption spectra of fluorcarletonite annealed at different temperatures in the 500-
551 1700 cm^{-1} range. The temperatures are given in Celsius degrees in the right side of the figure.
552 **Fig. 6**. IR absorption spectra of fluorcarletonite annealed at different temperatures in the OH
553 stretching vibration region. The temperatures are given in Celsius degrees in the right side of the
554 figure.
555

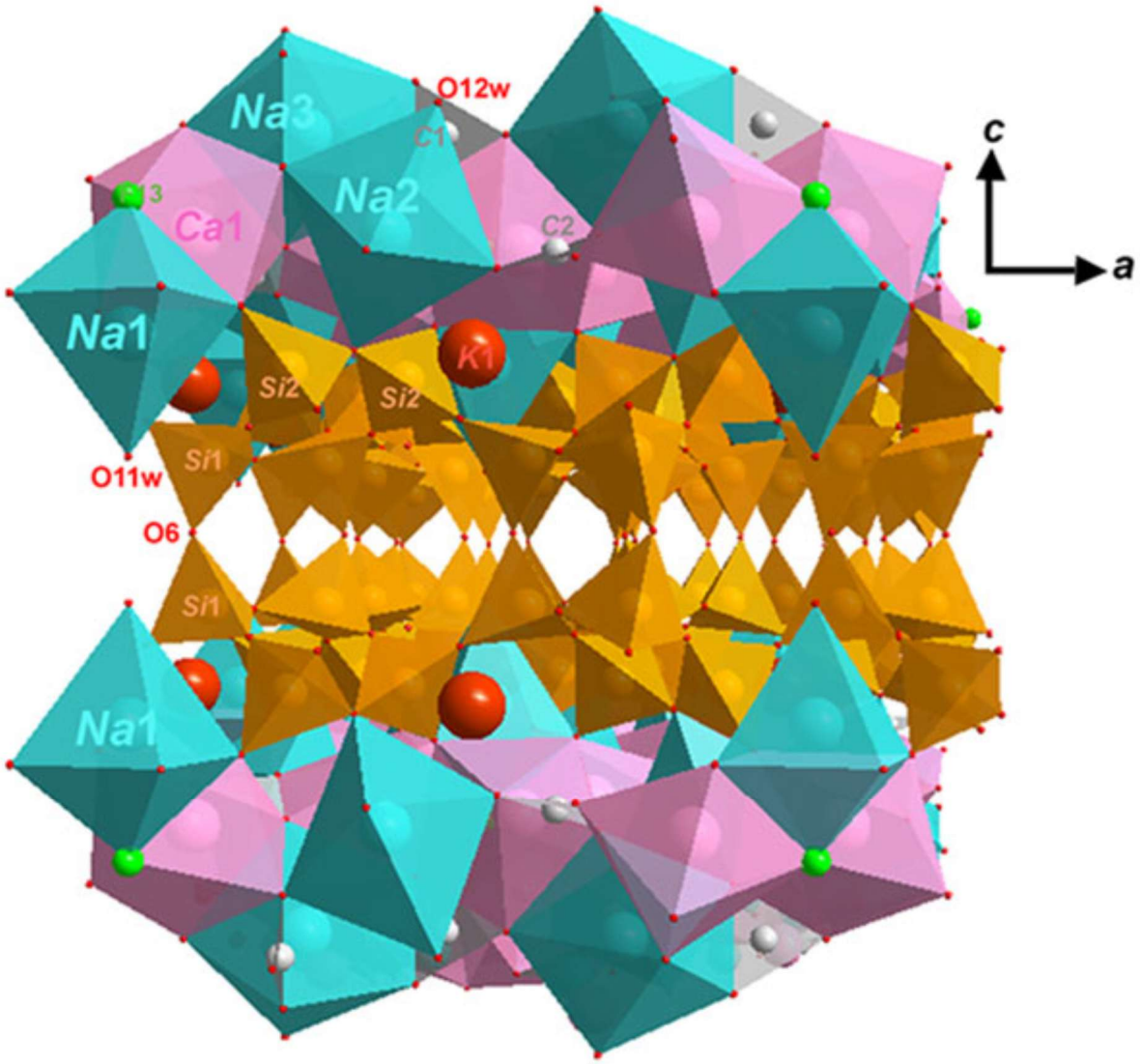

556

557 Figure 1

558

559

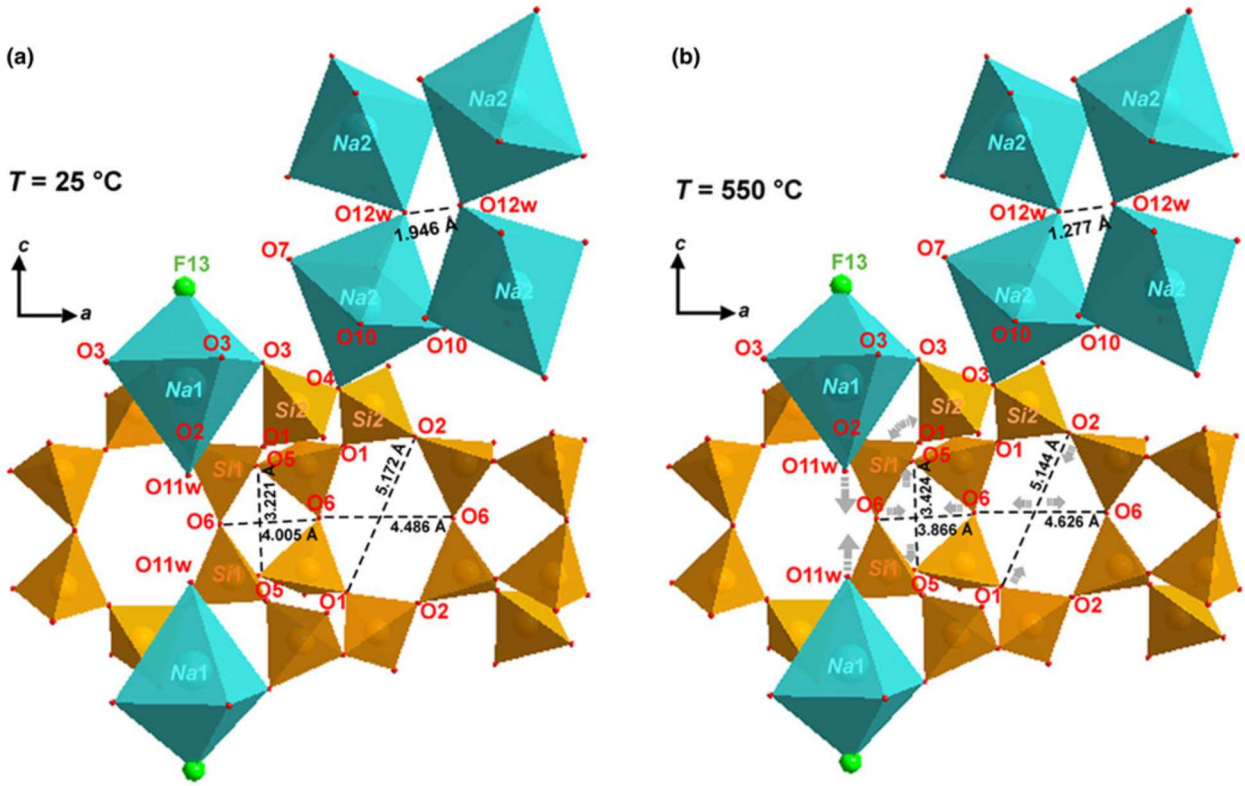

560

561 Figure 2

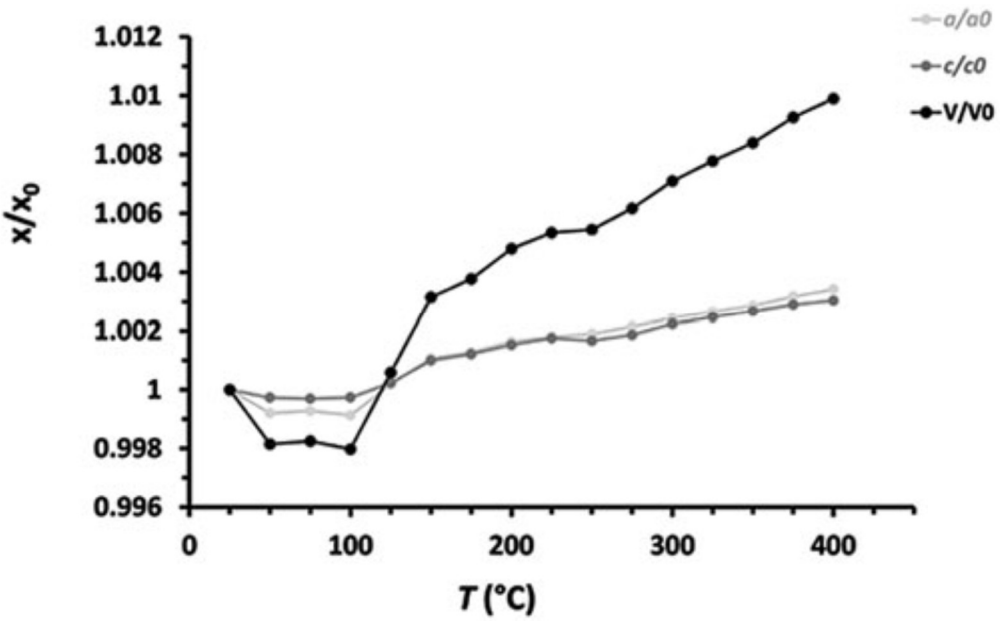

562

563

564 Figure 2

565

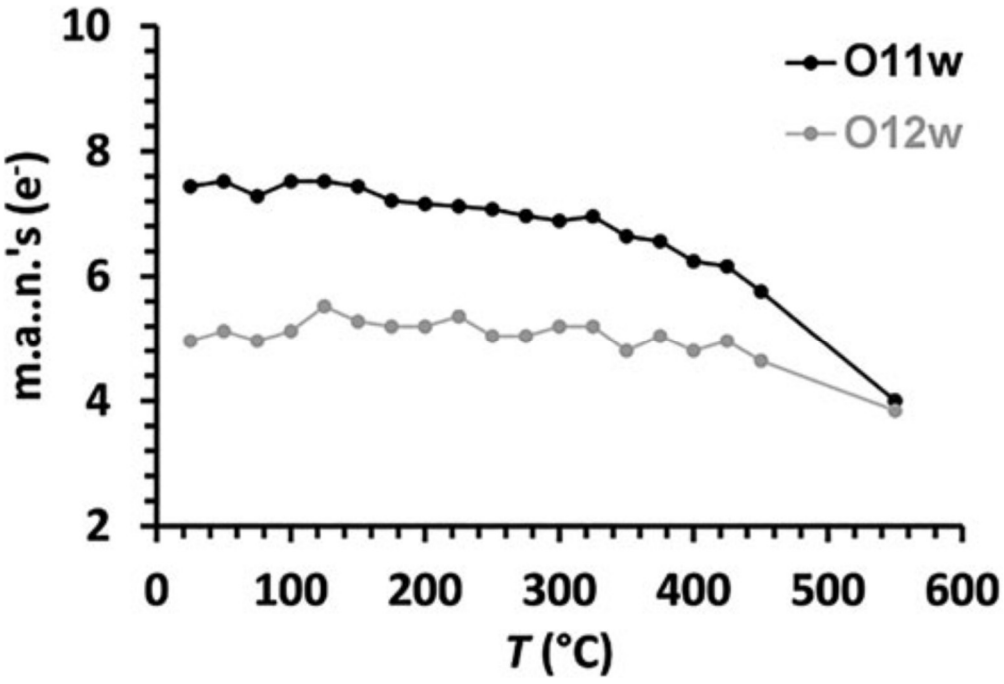

566

567 Figure 4

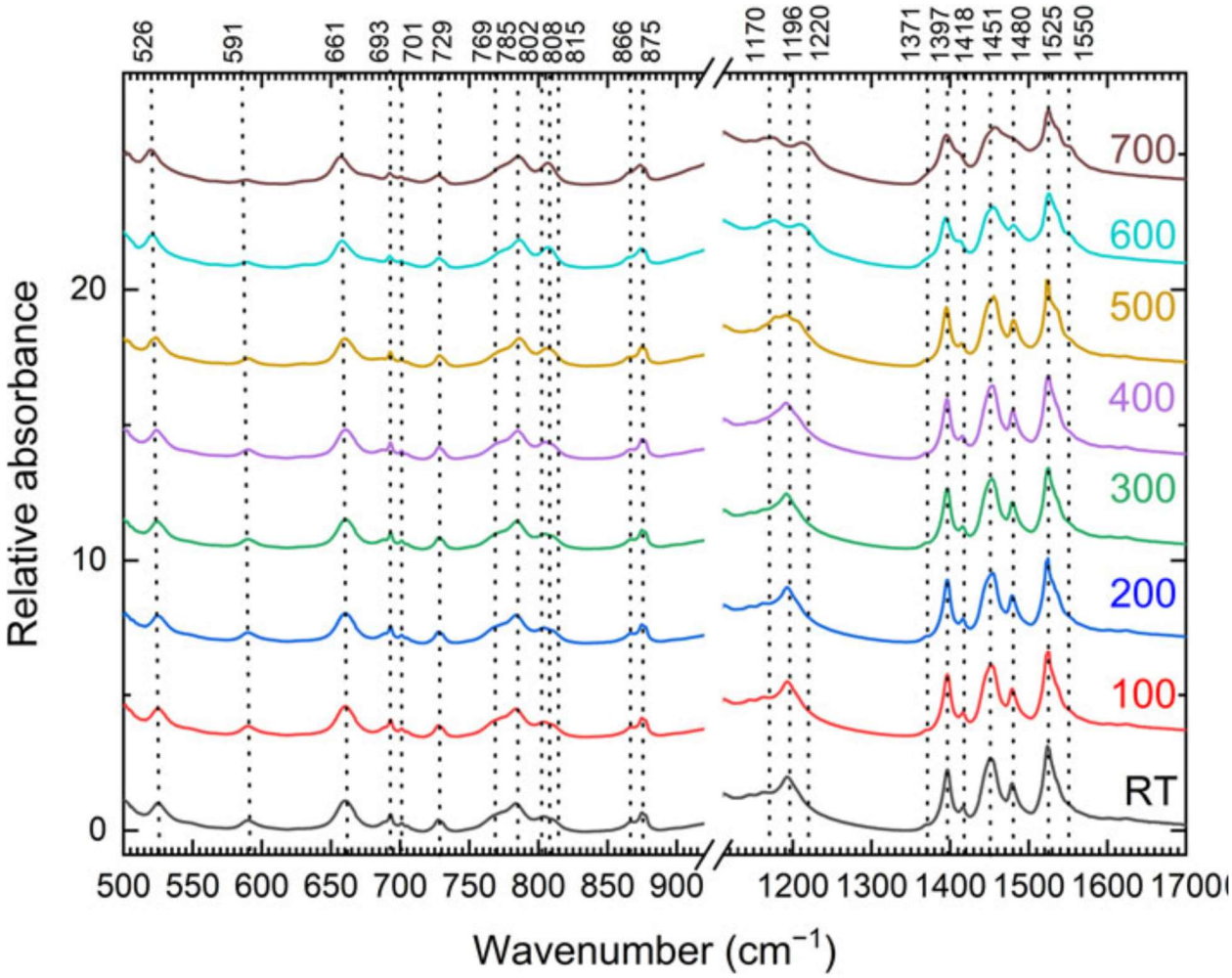

568

569 Figure 5

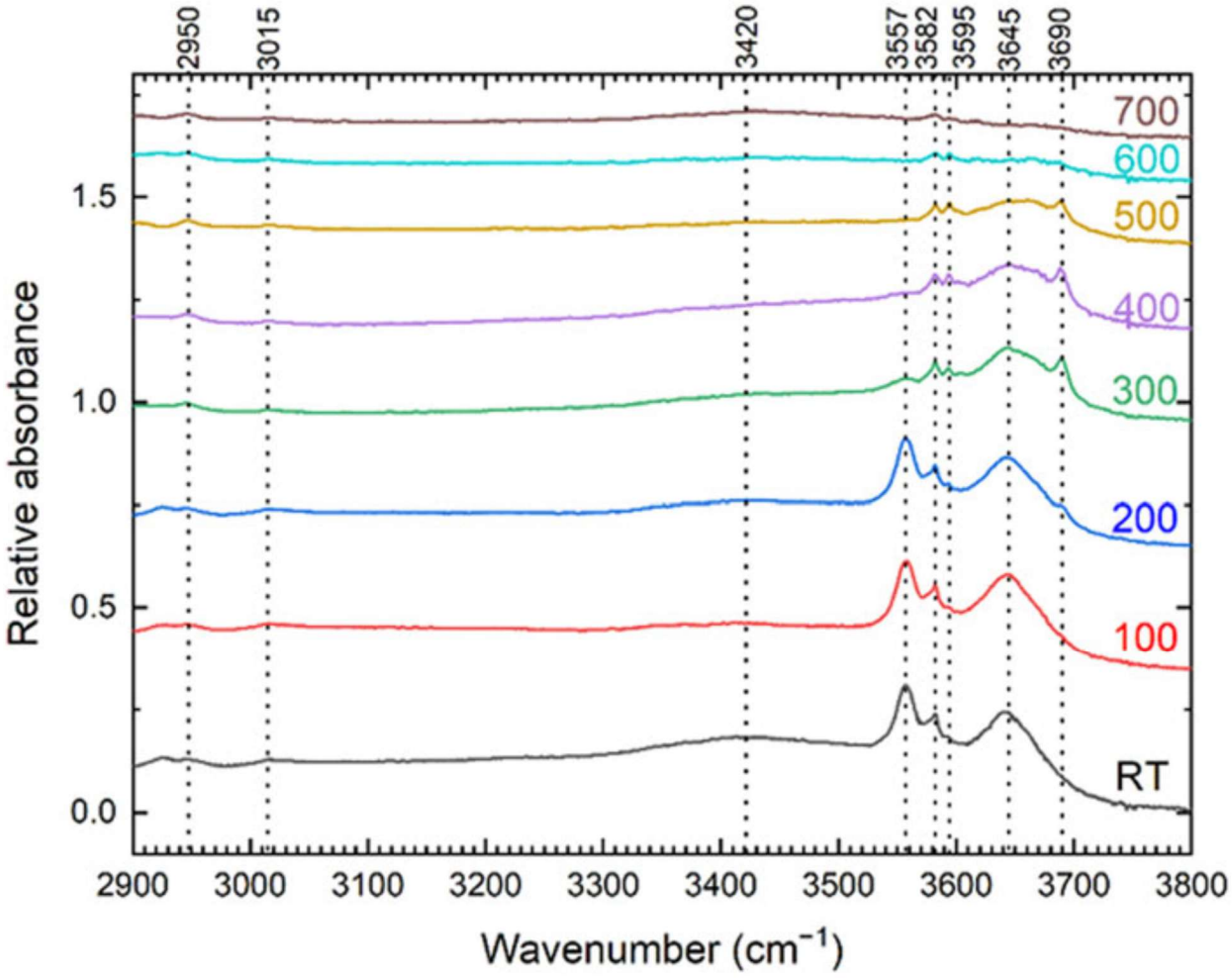

Figure 6

Table 1. Crystallographic data and experimental conditions for the studied fluorcarletonite at 25, 100, 200, 300 and 450 °C for Fcarl_1 crystal, and at 25 and 550 °C for Fcarl_2 crystal.

	Fcarl_1					Fcarl_2	
	25 °C	**100 °C**	**200 °C**	**300 °C**	**450 °C**	**25°C**	**550 °C**
Crystal data							
Space group	*P*4/*mbm*	*P*4/*mbm*	*P*4/*mbm*	*P*4/*mbm*	*P*4/*mbm*	*P*4/*mbm*	*P*4/*mbm*
a (Å)	13.2077(4)	13.1962(13)	13.2293(4)	13.2397(3)	13.2584(3)	13.2082(3)	13.2782(4)

c (Å)	16.7234(5)	16.7190(16)	16.7489(6)	16.7609(5)	16.7822(4)	16.7219(4)	16.8151(4)
V (Å^3)	2917.3(2)	2911.4(6)	2931.3(2)	2938.01(16)	2950.06(15)	2917.25(15)	2964.68(19)
Data collection							
Measured reflections	18888	18945	49275	55109	55439	18476	18723
Independent reflections	2444	2457	3826	3847	3860	2340	2386
$R_{merging}$ [$R_{(int)}$] (%)	8.1	8.4	6.3	6.5	6.7	6.6	7.1
h_{min}, h_{max}	-18, 17	-19,17	-21, 22	-22, 22	-22, 22	-18, 18	-18, 18
k_{min}, k_{max}	-18, 12	-18,11	-21, 15	-22, 15	-22, 15	-18, 10	-10, 18
l_{min}, l_{max}	-23, 23	-23,22	-27, 27	-27, 27	-27, 27	-22,23	-22, 22
Refinement							
Reflections used ($I > 3\sigma(I)$)	1736	1700	2573	2520	2387	1742	1632
No. of refined parameters	144	144	144	144	144	144	144
Goof[a]	1.121	1.111	1.049	1.018	0.999	1.022	1.018
R_1[b] [on F] (%)	3.34	3.43	3.07	3.04	3.15	2.83	3.04
wR_2[c] [on F^2] (%)	4.30	4.29	3.17	3.52	3.81	3.14	3.52
$\Delta\rho_{min}/\Delta\rho_{max}$ (e^-/Å^3)	-0.62, 0.79	-0.64, 0.59	-0.51, 0.67	-0.76, 0.77	-0.57, 0.55	-0.57, 0.65	-0.76, 0.77

Note: [a]Goodness of fit = $[\Sigma[w(F_o^2-F_c^2)^2]/(N-p)]^{1/2}$, where N and p are the number of reflections and parameters, respectively. [b]$R_1 = \Sigma[|F_o| - |F_c|]/\Sigma|F_o|$. [c]$wR_2 = [\Sigma[w(F_o^2-F_c^2)^2]/\Sigma[w(F_o^2)^2]]^{1/2}$, w = 1.0/[A[0]*T[0]'(X)+A[1]*T[1]'(X) ... +A[NP-1]*T[NP-1]'(X)] (Chebyshev optimized weights). The optimized parameters for each refinement are reported in the deposited Crystallography Information Files.

Table 2. Selected bond distances (Å) derived from the structure refinement of the studied fluorcarletonite at 25 and 450 °C (Fcarl_1 crystal), and at 550 °C (Fcarl_2 crystal).

	Fcarl_1		**Fcarl_2**
	25 °C	**450 °C**	**550 °C**
*Si*1-O1	1.593(2)	1.5887(16)	1.586(3)
*Si*1-O2	1.5954(19)	1.5958(14)	1.589(2)
*Si*1-O5	1.6206(12)	1.6179(9)	1.6149(15)
*Si*1-O6	1.6122(11)	1.6078(8)	1.6059(12)
<*Si*1-O>	1.605(1)	1.603(4)	1.599(1)
*Si*2-O1	1.626(2)	1.6197(15)	1.622(3)

*Si*2-O2	1.6291(19)	1.6250(14)	1.626(2)
*Si*2-O3	1.5764(19)	1.5765(13)	1.573(2)
*Si*2-O4	1.6286(11)	1.6289(8)	1.6276(13)
<*Si*2-O>	1.615(1)	1.613(2)	1.612(1)
*Na*1-O3 (×4)	2.347(2)	2.3854(15)	2.408(3)
*Na*1-F13	2.620(4)	2.623(4)	2.637(6)
*Na*1-O11w	2.349(7)	2.437(11)	2.59(3)
<*Na*1-O,F>	2.393(2)	2.434(3)	2.477(2)
*Na*2-O4	2.464(3)	2.498(3)	2.520(5)
*Na*2-O7 (×2)	2.392(2)	2.4046(19)	2.416(3)
*Na*2-O10 (×2)	2.345(2)	2.371(2)	2.384(4)
*Na*2-O12w	2.886(3)	3.065(16)	3.16(2)
<*Na*2-O>	2.471(2)	2.519(1)	2.547(4)
*Na*3-O7 (×4)	2.548(2)	2.568(2)	2.581(3)
*Na*3-O8 (×2)	2.396(3)	2.418(3)	2.419(4)
*Na*3-O9 (×2)	2.544(3)	2.569(3)	2.583(5)
<*Na*3-O>	2.509(1)	2.531(1)	2.541(2)
*Ca*1-O3	2.3757(19)	2.3875(14)	2.396(2)
*Ca*1-O3’	2.4388(18)	2.4526(14)	2.461(2)
*Ca*1-O7	2.526(2)	2.5493(16)	2.565(3)
*Ca*1-O7’	2.548(2)	2.5662(16)	2.577(3)
*Ca*1-O8	2.4504(5)	2.4579(4)	2.4628(7)
*Ca*1-O9	2.4333(9)	2.4531(8)	2.4683(13)
*Ca*1-O10	2.410(2)	2.4176(18)	2.416(3)
*Ca*1-F13	2.5054(7)	2.5129(5)	2.5152(9)
<*Ca*1-O,F>	2.461(2)	2.474(1)	2.483(2)
*K*1-O2 (×4)	3.205(2)	3.2269(16)	3.240(3)
*K*1-O5 (×2)	2.943(3)	2.939(2)	2.938(4)
*K*1-O10 (×4)	2.800(2)	2.816(2)	2.820(3)
<*K*1-O>	2.991(1)	3.005(1)	3.012(1)
*C*1-O7 (×2)	1.282 (3)	1.2864 (19)	1.282(3)
*C*1-O9	1.293 (5)	1.278 (3)	1.265(6)
*C*2-O10 (×2)	1.276 (3)	1.272 (2)	1.267(3)
*C*2-O8	1.301 (4)	1.299 (4)	1.304(6)

Table 3. Selected anion bond distances (Å) and angles (°) derived from the structure refinement of the studied fluorcarletonite at 25, 100, 200, 300 and 450 °C (Fcarl_1 crystal), and at 550 °C (Fcarl_2 crystal).

	25 °C	100 °C	200 °C	300 °C	450 °C	550 °C
O11w-O11w'	2.823(13)	2.806(15)	2.790(12)	2.756(14)	2.60(2)	2.26(6)
O12w-O12w'	1.95(4)	1.85(5)	1.76(4)	1.67(4)	1.49(5)	1.28(7)
O6-O6	4.005(6)	3.986(6)	3.987(4)	3.965(4)	3.924(5)	3.867(8)
O5-O5	3.221(5)	3.228(6)	3.261(4)	3.288(4)	3.342(5)	3.424(8)
O1-O2	2.581(3)	2.578(3)	2.5822(19)	2.5816(19)	2.578(2)	2.581(4)
O5-Ô6-O5	75.19(6)	75.53 (7)	76.11(4)	76.97(5)	77.99(5)	81.03(9)
O2-Ô1-O3	100.43(9)	100.67(9)	100.82(6)	101.10(6)	101.31(7)	102.0(1)

Table 4. Comparison between calculated and experimental values of infrared absorption bands of fluorcarletonite at room temperature and after heating at 700 °C. The band assignment is given basing on *ab initio* calculation.

Infrared band (cm^{-1})			Assignment
Experimental			
25 °C	700 °C	Calculated	
			O-Si-O bending + O12w-H libration
526	523	528	
			O11w-H libration + O-Si-O bending
591	587	602	
			O-Si-O bending + O12w-H libration
661	655	671	
			CO_3(*C*1, *C*2) bending + O11w-H libration
693	693	698	
			*C*1O_3 bending
701	701	701	
			O-Si-O bending + O11w-H libration
729	729	727	
			O-Si-O bending
769	769	765	
			O-Si-O bending
785	787	770	
			O11w-H + O12w-H libration
802		789	
			O-Si-O bending
808	808	794	
			O12w-H libration
815			
866	866	822 - 831	*C*1O_3 + *C*2O_3 bending (out-of-plane)
875	875		
			Si-O stretching
1047	1047	1007, 1039, 1056	
			Si-O stretching
1147	1147	1129	
			Si-O stretching
1170	1170	1139	
			Si-O stretching
1196	1196	1168	

			Si-O stretching
1120	1120	1180	*C*2O_3 stretching
1397	1397	1397	*C*2O_3 stretching
1418	1418	1411	*C*1O_3 stretching
1451	1451	1458, 1460	*C*1O_3 stretching
1480	1480	1474	*C*1O_3+*C*2O_3 stretching
1525	1525	1523, 1524	
1550	1550	1568 - 1606	O11w-H + Ow12-H bending
1600	1600		O11w-H stretching
3420	3420	3419	O11w-H stretching
3557	-	3517	O12w-H stretching
3582	3582	3571	O6-H stretching
-	3595	3584	O12w-H stretching
3645	3645	3632	O-H stretching
-	3690	3700	